LTE NLOS Navigation and Channel Characterization

Whiton, Russ; Chen, Junshi; Tufvesson, Fredrik

LTE NLOS Navigation and Channel Characterization

Russ Whiton, *Lund University, Volvo Cars*

Junshi Chen, *Lund University, Terranet AB*

Fredrik Tufvesson, *Lund University*

BIOGRAPHY

Russ Whiton Russ Whiton is a Senior Hardware Engineer at Volvo Car Corporation and an industrial PhD student at Lund University. He received his Bachelor's Degree in Electrical Engineering from Gonzaga University in 2008 and his M.Sc. in Electrical Engineering from Lund University in 2012. He has worked in the telecommunications and automotive industries. His research interests include localization and wireless communications.

Junshi Chen Junshi Chen received his M.Sc. from Beijing Jiaotong University in 2005. He worked for Huawei to develop 2G to 5G physical layer algorithms from 2005 to 2017. In 2017, he joined Terranet AB in Sweden and is currently an industrial PhD student at Lund University. His research interests include wireless signal characterization, signal processing and radio-based positioning.

Fredrik Tufvesson Fredrik Tufvesson is professor of radio systems at Lund University. His main research interest is the interplay between the radio channel and the rest of the communication system with various applications in 5G/B5G systems such as massive MIMO, mm wave communication, vehicular communication and radio-based positioning.

ABSTRACT

Navigation with terrestrial wireless infrastructure is appealing to overcome geometrical limitations of satellite navigation for users in environments with limited sky views. However, terrestrial signals are also prone to multipath that can result in angular and range estimates that are not representative of actual transmitter-receiver geometry. In this paper, some of these propagation effects are quantified for a particular urban non line-of-sight (NLOS) scenario, based on measurements of downlink reference symbols transmitted by a commercial Long Term Evolution (LTE) base station (eNodeB) and received by a massive antenna array mounted on a passenger vehicle. Empirical results indicate that large-scale statistics for a user making multiple passes through the same urban environment look similar when represented in terms of angles and delays despite changes in orientation and drive direction. Additionally, it is demonstrated that multipath effects can be utilized advantageously; it is possible to estimate not only user position but also orientation through wireless fingerprinting.

I. INTRODUCTION

The most well-known and widely-used wireless navigation systems are Global Navigational Satellite Systems (GNSS), including the United States Department of Defense's Global Positioning System (GPS), that provide positioning references in semi-synchronous Medium Earth Orbit (MEO). Users on the ground with an inexpensive GNSS receiver and antenna can localize themselves in real-time in a global reference frame with meter-level accuracy without external augmentation or sensor fusion. However, indoor areas, areas with heavy foliage, urban canyons, and other places with obstructed views of the sky face tougher challenges for achieving accurate and robust navigation.

Numerous applications would benefit from GNSS-like localization capabilities in these environments. The most promising technology for replicating the ubiquity of GNSS is cellular communication, which is rolled out across the world and offers generous bandwidth and transmit power (Kassas et al., 2017). For these reasons, use of cellular communication has been explored and deployed as a GNSS complement or alternative for decades (del Peral-Rosado et al., 2017), with a focus on base station localizing of User Equipment (UE). While not widely commercially deployed, Fourth Generation (4G) Long-Term Evolution (LTE) systems introduced several Positioning Reference Symbols (PRS) already in 3rd Generation Partnership Project (3GPP) Release 9. Fifth-Generation (5G) systems built on 3GPP Release 16 have new dedicated signals for both uplink and downlink positioning using angles and delays (Dwivedi et al., 2021).

However, the use of cellular signals for localization in GNSS-challenged environments is not trivial. The physical mechanisms of wave propagation mean that the dominant energy contribution of the received channel response may not correlate strongly with the physical transmitter-receiver geometry, resulting in systematic biases of delay estimates (Aditya et al., 2018). Researchers have expressed significant interest in determining how LTE, and specifically LTE based on Time-of-Arrival (TOA), performs

in multipath environments through both simulation and measurement. Much work has been done to understand the large-scale statistics of multipath propagation (Müller et al., 2016), and to characterize various techniques for TOA estimation (Wang and Morton, 2020). Innovative techniques have been introduced to mitigate multipath at a signal processing level, including multipath-estimating delay locked loops (Wang and Morton, 2020), machine learning (Orabi et al., 2021), or even at an application level through environmental maps (Strandjord et al., 2021). Another school of thought is to try to exploit the environmental information embedded in multipath propagation for improved fingerprinting (Vieira et al., 2017), Simultaneous Location and Mapping (SLAM) (Gentner et al., 2016), or for establishing a shared reference frame among users (Ulmschneider et al., 2021).

In this work, physical channel behavior is characterized in terms of TOA and Angle-of-Arrival (AOA) statistics for a particular urban canyon scenario. For a passenger vehicle following a similar trajectory through multiple passes of an urban canyon environment, propagation statistics show consistency when expressed in these domains. Furthermore, equipped with an advanced understanding of the channel, multipath propagation is used opportunistically for improved navigation. A channel fingerprint is introduced that enables a passenger vehicle to predict not only position, but orientation from a single sector of one eNodeB operating at 2.6 GHz in NLOS conditions. While previous work has used external sensory data to augment fingerprints, see, e.g., Table IV in (Burghal et al., 2020) regarding "Side Information", one insight absent from fingerprinting literature is that information about UE orientation is embedded in channel fingerprints, even if angular resolution on the UE side may be limited for many practical scenarios. Our research contributions are as follows:

- A channel fingerprint utilizing multipath propagation is introduced to enable estimation of both position and heading, and the concept is verified with measurement data recorded in an urban canyon of signals received from a commercial eNodeB.

- Delay biases and, owing to the advanced spatial resolution of the measurement system employed, angular spreads are quantified for this NLOS scenario.

The manuscript is organized as follows: basics of LTE signal demodulation and channel representation are introduced in Section II; details of the measurement campaign, including the measurement system and drive route are provided in Section III. The estimators are briefly described in Section IV; channel statistics and estimator performance from the test drive are presented in Section V; and finally, conclusions are drawn in Section VI.

II. CHANNEL CHARACTERIZATION

1. LTE Downlink Channel State Information

Numerous synchronization signals are frequently broadcast in LTE, including Primary Synchronization Symbols (PSS) and Secondary Synchronization Symbols (SSS) which allow the UE to synchronize with network time and deduce Cell Identification Numbers (CID). Cell-Specific Reference Signals (CRS) are used by the UE for channel estimation for coherent demodulation and to obtain Channel State Information (CSI) (Dahlman et al., 2013). CRS are particularly appealing for navigation because they span the channel bandwidth, are transmitted frequently, and unlike PRS they are transmitted regardless of network operator configuration. The sequences are known *a priori* to the UE, which can multiply the Discrete Fourier Transform (DFT) of the received signal with the conjugate of the known transmitted signal to obtain the CSI estimate. For the multiple-receive antenna system introduced in Section III, this is done on a per-antenna basis, and estimated CSI is expressed as a complex value at each time index t per subcarrier, per antenna, $\hat{\mathbf{F}}_t$:

$$\hat{\mathbf{F}}_t \in \mathbb{C}^{M \times S} \tag{1}$$

Where M is the number of receive antennas and S is the number of subcarriers.

2. Channel Representation

CSI is a raw form of channel information, and propagation channels are often modeled as the superposition of a discrete number of plane waves, including a direct Line-of-Sight (LOS) path and Specular Multipath Components (SMCs). If the LOS path is attenuated to the point of being unresolvable but other components are resolvable, it is called a NLOS scenario. Such a model is useful for many tasks in communication and localization, but there are several limitations. For one, the plane wave model alone necessarily discards some of the energy contained in the Channel Impulse Response (CIR) from propagation mechanisms other than specular reflection, or even specular reflection that is unresolvable for a given channel bandwidth and measurement aperture. So-called Diffuse Multipath Components (DMCs), which can be understood as the superposition of many components of lesser power that are too small to effectively estimate individually, also contain information. Another problem is that decomposition into plane waves requires the additional step of channel estimation which requires processing power, particularly for methods

based on expectation maximization or subspace searches. Yet another problem in plane wave modeling is that model order number can vary dramatically, which is consequential for both communication and localization.

A somewhat less cumbersome approach to decompose the channel into a domain with intuitive and sparse properties, an approach without matrix inversions or subspace searches, is to use a matched filter (Luo et al., 2021). The effects of the antenna pattern can be compensated for through matrix multiplication with the Hermitian transpose of the per-antenna measured complex radiation pattern $\mathbf{A}$, which is measured for M antennas at the center frequency in discrete steps of $\Delta\theta$ for elevation angles θ and steps of $\Delta\phi$ for azimuthal angles ϕ, e.g., (Landmann and Del Galdo, 2004):

$$\mathbf{A} \in \mathbb{C}^{M \times ((\frac{\pi}{\Delta\theta}+1)*(\frac{2\pi}{\Delta\phi}))} \tag{2}$$

Similarly, decomposition into the time domain is done through multiplication with the conjugate of the matrix of per-subcarrier phase shifts $\mathbf{D}$ at frequency indexes of the subcarriers f_1 to f_S for the desired length of the channel into T discrete time steps from τ_0 to τ_{T-1}:

$$\mathbf{D} = \begin{bmatrix} 1 & e^{2\pi f_1 \tau_1} & \dots & e^{2\pi f_1 \tau_{(T-1)}} \\ \vdots & \vdots & \ddots & \vdots \\ 1 & e^{2\pi f_S \tau_1} & \dots & e^{2\pi f_S \tau_{(T-1)}} \end{bmatrix} \in \mathbb{C}^{S \times T} \tag{3}$$

By performing a matrix multiplication of the CSI $\hat{\mathbf{F}}$ with the Hermitian transpose of the combined antenna pattern across antennas, $\mathbf{A}^{\mathbf{H}}$, and the conjugate per-subcarrier phase shifts $\mathbf{D}^*$, the CSI is transformed into an angular-delay bin channel estimate $\hat{\mathbf{Y}}$, with granularity according to the sampling interval of the antenna pattern and delay according to the per-subcarrier phase shift matrix $\mathbf{D}$:

$$\hat{\mathbf{Y}}_t = \mathbf{A}^{\mathbf{H}} \hat{\mathbf{F}}_t \mathbf{D}^* \in \mathbb{C}^{((\frac{\pi}{\Delta\theta}+1)*(\frac{2\pi}{\Delta\phi})) \times T} \tag{4}$$

Rearranging into a three-dimensional tensor $\hat{\mathbf{Z}}_t$ in the order of elevation, azimuth and delay:

$$\hat{\mathbf{Y}}_t \in \mathbb{C}^{((\frac{\pi}{\Delta\theta}+1)*(\frac{2\pi}{\Delta\phi})) \times T} \rightarrow \hat{\mathbf{Z}}_t \in \mathbb{C}^{(\frac{\pi}{\Delta\theta}+1) \times (\frac{2\pi}{\Delta\phi}) \times T} \tag{5}$$

This matrix multiplication, while still computationally intensive for a massive antenna array with narrow sampling of the complex antenna pattern, yields an intuitive result for viewing of the channel in the angular and delay domains and is well-suited for rich multipath channels at lower frequencies that are not well-characterized by plane-wave modeling.
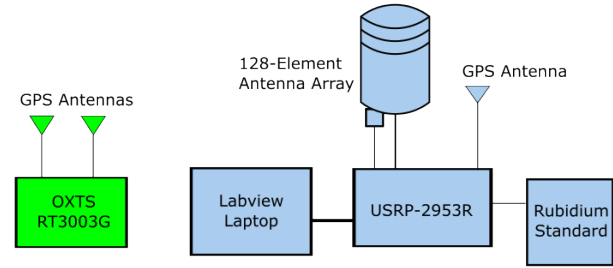
III. MEASUREMENTS FROM LTE ENODEB

1. LTE Signal Measurement and Hardware

Signals transmitted by a commercial LTE eNodeB were recorded using a USRP-2593R Software Defined Radio (SDR) and LABView from National Instruments. PSS and SSS were used to establish frame timing, and PSS/SSS/CRS symbols in the time domain were subsequently logged on a test laptop for offline data processing. The USRP also included a GPS receiver which was used for synchronization with GPS time and as a point of comparison for Results in Section V. The frequency reference for the USRP was generated by an FS725 Rubidium Frequency Standard from Stanford Research Systems (disciplined by a GPS receiver-generated 1 pulse-per-second output prior to testing) to provide a more stable oscillator reference than the USRP's internal oscillator. The SDR served as both a receiver and an antenna switch controller, connected to a 128-element (4 vertical rings of 16 patch antennas with 2 cross-polarized elements per patch) Stacked Uniform Circular Array (SUCA) , which switched at the rate of 2 CRS symbols per antenna[1], or equivalently 0.5 ms. The complete measurement set-up is depicted in Figure 1.

Ground truth vehicle pose, including orientation, was generated by a dual-constellation, dual-antenna, dual-frequency Oxford Systems RT3003G system with Post-Processed Real-Time Kinematics (RTK). A GoPRO MAX $360°$ camera was mounted on the top of the antenna array to check for data irregularities.

---

[1]Note that switching at the rate of CRS symbol transmission imposes strict limitations on driving speed to avoid exceeding channel coherence time. Sampling antennas in parallel would negate limitations in speed, but significantly increase data logging or real-time data processing requirements.

Figure 1: (Left) Photo of test vehicle. (Right) Block diagram of measurement set-up.

2. Drive Route

A deep urban environment and LTE eNodeB were selected for testing with a presumption that various propagation mechanisms would contribute appreciable amounts of energy to the CIR, including diffraction over rooftops, wave guiding down streets, scattering from surrounding objects including other vehicles and specular reflections from smooth surfaces. At all points along the test route the direct path to the transmitter was heavily attenuated by multi-story buildings. Reception of GNSS signals was possible in this environment, but measurements derived from GPS-only measurements exhibited errors on the order of tens of meters, as shown in Section V. The ground truth system benefitted from post-processing (smoothing), inertial fusion and the Eastern section of the route which had an open sky view on three sides.

The geometry of the drive laps relative to the transmitting eNodeB is shown on the left side of Figure 2. Two laps were driven clockwise (laps two and three, defined as the positive direction for odometry in Section V) and two were driven counter-clockwise (one and four). There are lateral position offsets on the order of a few meters for the Eastern and Western sections of the route which are multi-lane. The route spanned slightly more than 100 meters North-South and East-West, and each lap was about 400 meters of driven distance. Average speed was about 1 meter/second to avoid exceeding channel coherence time for the slowly switched system.
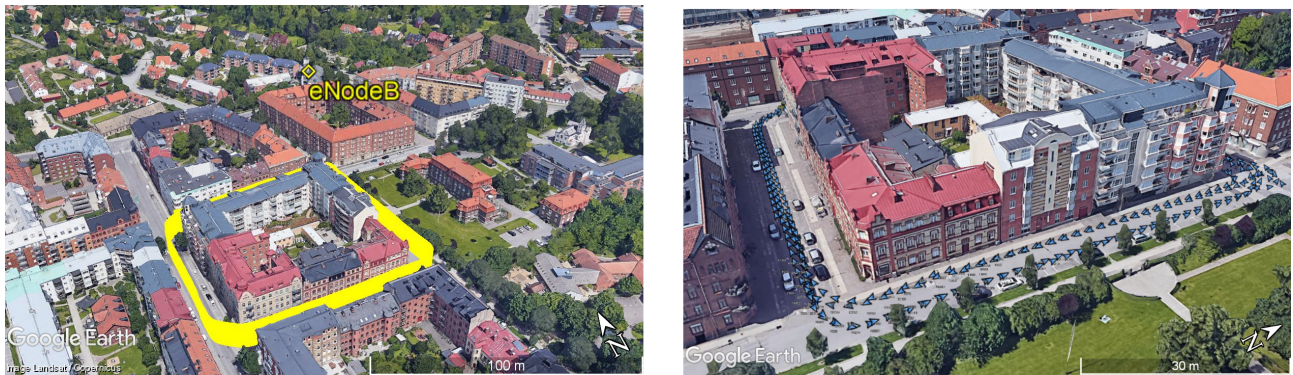
Figure 2: (Left) Visualization of drive lap area and transmitting eNodeB in Lund, Sweden (approx. location 55.71°N, 13.19°E). (Right) Position and heading for selected snapshots on each of the four laps to illustrate lateral offsets and drive direction differences. Images created with Google Earth.

There is uncertainty in the absolute position of the phase center of the transmitting eNodeB, as well as with the time-varying absolute clock offset beween the measurement system and eNodeB. A manual calibration was done in post-processing to try to refine estimates of the antenna phase center's three-dimensional location and a static absolute clock offset, based on LOS data collected before and after the four drive laps from approximately the same starting point. Visual results in the delay and azimuthal domains, presented in Section V, show minimal variation over time, but these ambiguities mean that the absolute numbers can be considered accurate on a meter-level at best. The measurement system's absolute time synchronization with the disciplined Rubidium oscillator appears to be adequate for at least a visual analysis. The oscillator of the eNodeB was unknown because it was a commercially operating mobile network, and the test system oscillator was subject to vibration and changes in temperature over a period of about an hour.

This should not be confused with ambiguity in the position domain for the vehicle position estimator presented in Section IV,

because ground truth estimates are accurate on a centimeter-level and not derived from eNodeB position. Rather, the opposite is the case that eNodeB position is derived from vehicle pose that is well-anchored in a geodetic frame.

IV. ESTIMATORS FOR CHANNEL REPRESENTATION AND LOCALIZATION

1. Estimator for TOA Channel Characterization

The LTE positioning problem is often formulated as a trilateration problem where ranges (pseudoranges including transmitter-receiver clock mismatch, in practice) are taken to known reference points. TOA estimators of varied complexity and performance have been considered for LTE estimation, and previous work has considered performance as a function of signal-to-noise ratio and environmental conditions using Geometry-Based Stochastic Channel Models (GBSCMs) (Wang and Morton, 2020).

Using the measurement set-up described in Section III, a simple peak-detector p_{ranges} is implemented to estimate L delay peaks from d_1 to d_L for a CIR as shown in the left subfigure of Figure 3:

$$p_{ranges} : CIR \rightarrow \{d_1, d_2, ...d_L\} \tag{6}$$
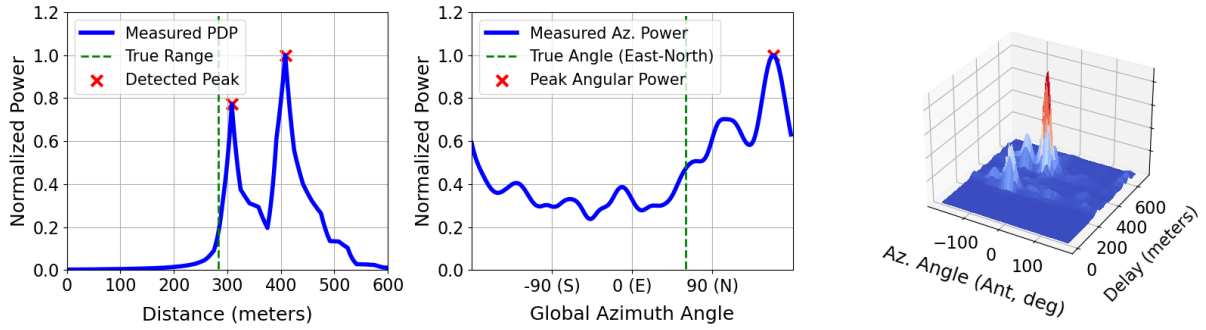
Figure 3: Channel data for one snapshot. (Left) CIR with peak detection. (Middle) Azimuthal spectra. (Right) Azimuthal-delay spectra in antenna reference frame.

Next, the CIR is generated as a compression across the tensor elements $\hat{z}_{(i,j,k),t}$ of $\hat{\mathbf{Z}}_t$ which compresses the channel into the time domain, and the delay bias κ_t per snapshot is calculated as the difference between the true distance at time t to the eNodeB η_t^{BS} and the first peak d_1:

$$\kappa_t = p_{ranges}(\sum_{i=1}^{I}\sum_{j=1}^{J} \hat{z}_{(i,j),t})_1 - \eta_t^{BS} \tag{7}$$

2. Estimator for AOA Channel Characterization

A similar analysis is done for AOA, a compression across the tensor elements $\hat{z}_{(i,j,k),t}$ of $\hat{\mathbf{Z}}_t$ in the dimensions of elevation and delay. The absolute difference in degrees ξ_t between the absolute peak angular power of the azimuthal spectra and the geometric angle to the eNodeB γ_t^{BS}, as is shown in the middle subfigure of Figure 3.

$$\xi_t = min(\gamma_t^{BS} - max(\sum_{i=1}^{I}\sum_{k=1}^{K} \hat{z}_{(i,j,k),t}), 2\pi - (\gamma_t^{BS} - max(\sum_{i=1}^{I}\sum_{k=1}^{K} \hat{z}_{(i,j,k),t}))) \tag{8}$$

3. CNN Estimator and Kalman Filter for Position and Heading Estimation

A Convolutional Neural Network (CNN) is used to generate estimations of two-dimensional position together with heading. The goal with the estimator f_{CNN} is to take a channel fingerprint $\mathbf{Y}_t$ and generate a three-dimensional measurement $\hat{\mathbf{y}}_t$ of UE pose including East-West position $\hat{y}_e$, North-South position $\hat{y}_n$ and heading angle $\hat{y}_\gamma$:

$$f_{CNN}(\mathbf{Y}_t) \rightarrow \hat{\mathbf{y}}_t = [\hat{y}_e, \hat{y}_n, \hat{y}_\gamma]^T \in \mathbb{R}^3 \tag{9}$$

Table 1: CNN Estimator Description

Parameter	Value
Input Layer Dimensions	90 x 82
Delay Range (meters / ns)	0 to 675 / 0 to 2083
Azimuthal Range (degrees)	-180 to 180
Delay Resolution (meters / ns)	8.2 / 25.4
Azimuthal Resolution (degrees)	4
CAP Layer 1 Filters / Weights	16 / 160
CAP Layer 2 Filters / Weights	32 / 4640
CAP Layer 3 Filters / Weights	64 / 18,496
Dense Layer 1 Weights	901,248
Dense Layer 2 Weights	8256
Kernel Size (All conv. layers)	3
Pool Size (All pooling layers)	2x2
Output Layer Shape	3
Trainable parameters	932,995

The SUCA antenna has significantly better resolution in the azimuthal domain than in elevation, so the input fingerprints are compressed in the elevation direction to reduce the computational complexity for both training and run-time. The parameters of the CNN are given in Table 1. Rather than performing three-dimensional convolutions on the tensor $\hat{\mathbf{Z}}_t$, the footprints used in this case, $\hat{\mathbf{Z}}_{az\_del,t}$, are two-dimensional in the azimuthal-delay domain, as shown in the right side sub-figure of Figure 3:

$$\hat{\mathbf{Z}}_{az\_del,t} = \sum_{i=1}^{I} \hat{z}_{(i,j,k),t} \tag{10}$$

Complete state estimates generated at each snapshot at discrete time t are filtered with an Extended Kalman Filter (EKF) employing a coordinated turn process model, where three of the parameters are observed directly by the output of the CNN, and velocity $\hat{x}_v$ and turn rate estimates $\hat{x}_\omega$ are treated as stochastic parameters, for a complete state vector $\hat{\mathbf{x}}_t = [\hat{x}_e, \hat{x}_n, \hat{x}_v, \hat{x}_\gamma, \hat{x}_\omega]^T$. The state estimates at each time step t of duration Δt = 75 ms are from a prediction step:

$$\hat{\mathbf{x}}_{t|t-1} = \begin{bmatrix} \hat{x}_{e,t-1} + \Delta t \cdot \hat{x}_{v,t-1} \cdot cos(\hat{x}_{\gamma,t-1}) \\ \hat{x}_{n,t-1} + \Delta t \cdot \hat{x}_{v,t-1} \cdot sin(\hat{x}_{\gamma,t-1}) \\ \hat{x}_{v,t-1} \\ \hat{x}_{\gamma,t-1} + \Delta t \cdot \hat{x}_{\omega,t-1} \\ \hat{x}_{\omega,t-1} \end{bmatrix} + \mathbf{w}_t \tag{11}$$

Where $\mathbf{w}_t$ is a zero-mean sequence with covariance $\mathbf{Q} = diag([q_e, q_n, q_v, q_\gamma, q_\omega])$. Observations are linear in the state space:

$$\hat{\mathbf{y}}_t = \begin{bmatrix} 1 & 0 & 0 & 0 & 0 \\ 0 & 1 & 0 & 0 & 0 \\ 0 & 0 & 0 & 1 & 0 \end{bmatrix} \hat{\mathbf{x}}_t + \mathbf{r}_t \tag{12}$$

Where $\mathbf{r}_t$ is zero-mean with covariance $\mathbf{R} = diag([r_e, r_n, r_\gamma])$.

V. RESULTS

1. Channel Measurements

A critical factor for localization using fingerprinting is whether the fingerprint representation is consistent across space and time. A fingerprint that is sensitive to minor perturbations in the environment will be of limited utility; the differences between data collection and run-time will make inferences less meaningful. Figure 4 shows the delay spectra for the four laps as a function of odometry (the x-axis is inverted for counter-clockwise drive laps). The Euclidian distance from the vehicle to the eNodeB antenna itself is shown in blue. There are visibly similar patterns in each of the laps both in terms of the absolute value of delay spectra and the relative spacing of the major energy contributions. Several lessons can be drawn from these results, both about the channel behavior and about the measurement system.
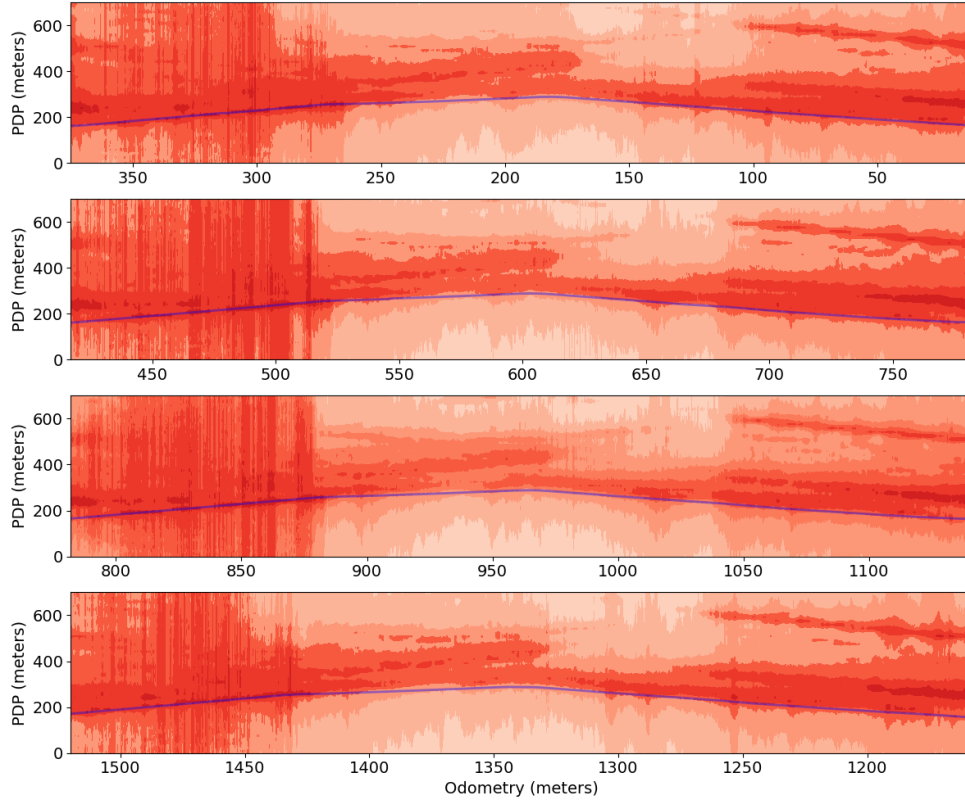
Figure 4: Power Delay Profile as a function of odometry from one sector of one eNodeB for four drive laps, as well as the Euclidian distance from the vehicle to the eNodeB (blue).

At the beginning of the route (the Eastern section) there is an apparent smearing of energy; it is an artifact of interference from another eNodeB that has strong signal power and a cell ID that entails transmission on the same resource blocks. Interference cancellation allows for data communication, but complicates propagation modeling for this section.

With regard to the channel behavior itself, the peaks of the delay spectra lag the Euclidian distance from the vehicle to the eNodeB, as expected for this NLOS scenario. Given the 20 MHz channel bandwidth with 200 subcarriers used in the estimation, it is unsurprising that an effective discrete representation of the channel under these conditions appears difficult, as propagation mechanisms other than specular reflection are contributing energy to the CIR and the resolution is limited. For an urban scenario with similar bandwidth and number of antennas, DMCs were previously found to comprise 10-30% of the impulse response energy (Sangodoyin et al., 2018). The last segment (Northernmost) part of the route shows strong multipath components with delay-distance components in excess of 300 meters from the early peaks. This is not surprising for LTE, which supports Cyclic Prefix (CP) lengths corresponding to over a kilometer of propagation distance even in normal CP mode. The consistency of the spacing between components shows that it is reasonable to infer information about position based on delay spreads, and provides further evidence that there is information which can be retrieved for localization (Niitsoo et al., 2019).

Figure 5 shows global (East-North) azimuthal spectra for the same drive laps. The spectra are again visibly consistent in spite of lateral offsets in the drive route and differences in driving direction. Strong discontinuities are visible that are consistent across drive laps, and at intersections the energy appears to shift compass directions, following the North-South and East-West layout of the surrounding buildings. This is highly consequential if AOA is to be used for state estimation, see, e.g., (Shamaei et al., 2018).

2. Bias Characterization

The biases of the TOA estimator and AOA estimators described in Section IV are shown in Figure 6. For the TOA estimator, a normal distribution with a mean of 30 meters and standard deviation of 12 meters is plotted for comparison. Previous work has utilized a skew-t distribution (Müller et al., 2016) with the intention of combining both LOS and NLOS scenarios, but of course the distribution parameters in that case will depend heavily on the mix of the two in the underlying data set. All measurements
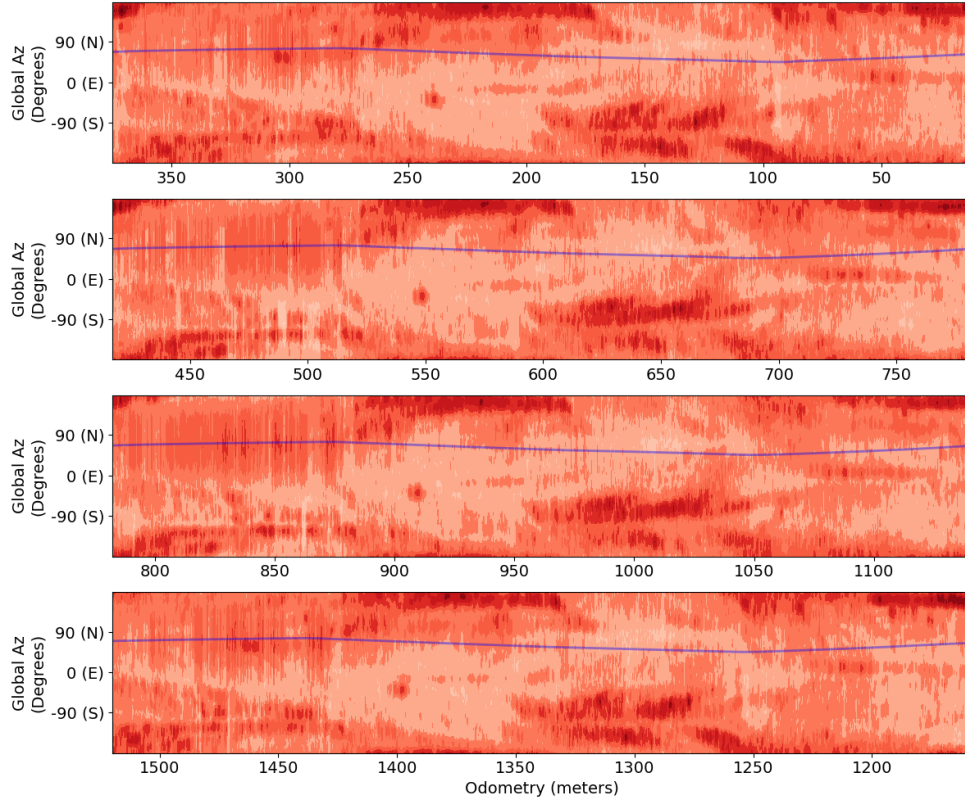
Figure 5: Azimuthal spectra for four laps as well as the calculated angle to the eNodeB (blue).

in this data set are NLOS.

Note that data from the Eastern section of the route, for which significant interference from a separate eNodeB was observed (visible on the left side of the laps in Figure 4), was excluded from the statistics because this interference results in distortion of the CIR and false local maxima when applying the peak detector p_{range}. Future work will employ better interference cancellation techniques to address this problem. The choice of peak detector applied to the time domain measurements is consequential, but was not found to significantly impact the shape of the results for these drives or to reduce lap-to-lap consistency.
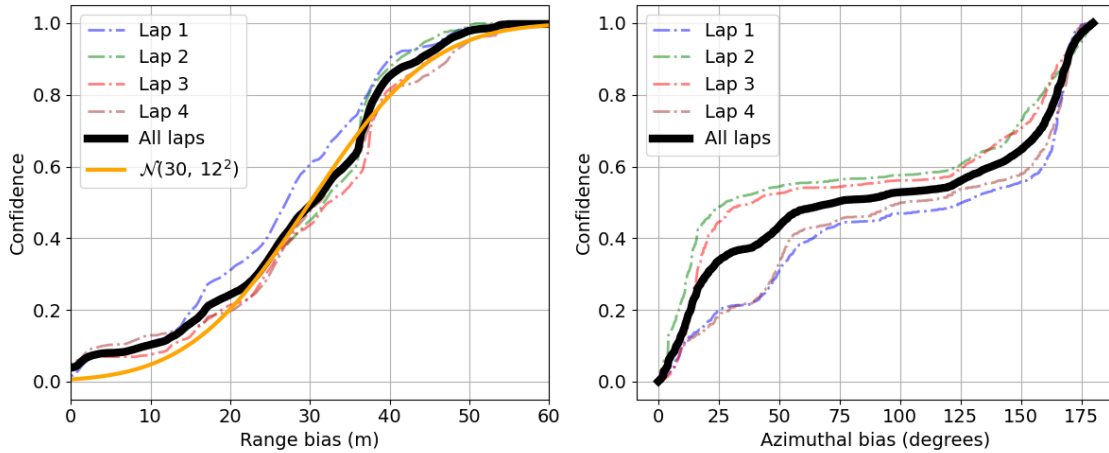

Figure 6: (Left) Cumulative distribution function of range biases κ_t. (Right) Cumulative distribution function of azimuthal biases ξ_t.

3. Localization with CNN

The results of the position and heading estimator described in Section IV.3 are shown in a map view and time series in Figure 7, both for the unfiltered and filtered estimates. Comparison with the GPS L1 receiver integrated into the SDR is also given as a reference.

From the map view, it is apparent that the estimator is capable of differentiating the different segments of the lap, but it suffers in differentiating the Northwest and Southeast corners. Part of the trouble in the Southeast corner may be attributable to interference from the other eNodeB. The settings of the filter in the SDR GPS receiver are opaque, but total position error is similar in this environment. One important advantage of the CNN estimator is that it provides independent heading estimates, as opposed to the SDR GPS receiver which must assume that the traversed path of the antenna corresponds with direction of travel without consideration for the vehicle body frame.
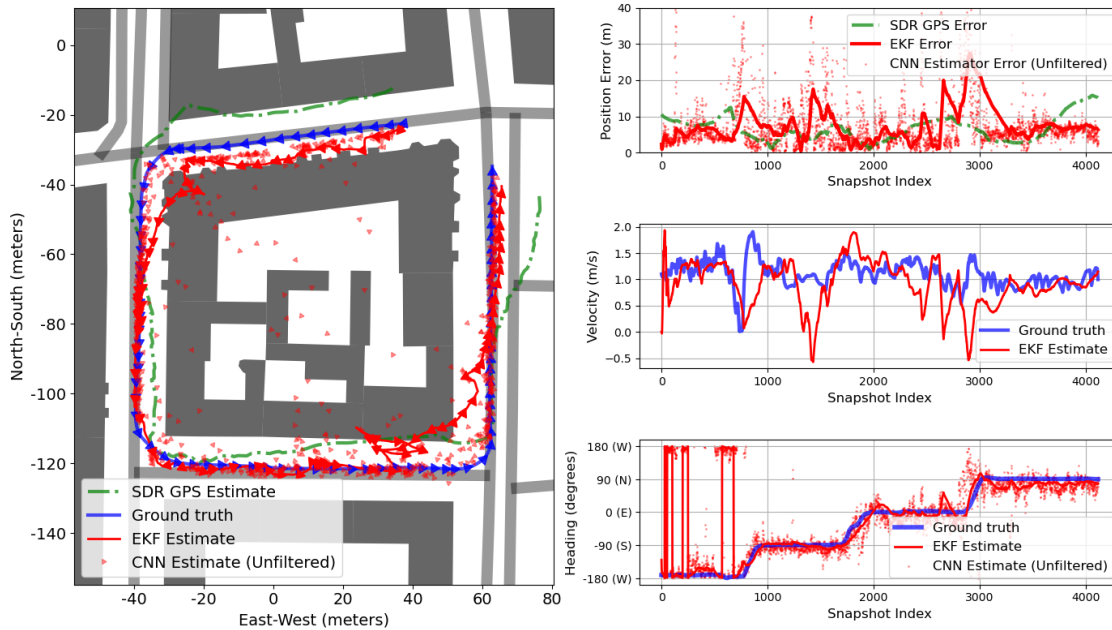
Figure 7: Results of position and heading estimation for filtered and unfiltered CNN estimates. (Left) Map view of fourth lap ground truth and estimates. (Right) Time series view of estimates.

Velocity estimates at the output of the estimator appear to be particularly poor, which is in part owing to the lack of observability of the parameter with this choice of motion model with measurements of position and heading. Augmentation with wheel odometry or inertial measurement would likely be effective at addressing this deficiency.

A cumulative distribution function of the errors in position and heading are shown in Figure 8. The position estimation of the CNN performs similarly to the SDR GPS receiver, but this is strongly influenced by the poor CNN performance in the section of the drive route that suffers from interference. CNN heading estimation appears to be effective for the unfiltered estimates, correctly estimating the direction of travel (less than 90° heading error) well over 95% of the time, which demonstrates that there is potential for fingerprinting to provide observations of more of the state vector than position alone. CNN estimates are based on 75 ms snapshots, but aggregation of energy into multiple snapshots would likely result in more stable estimates at the expense of longer update times.

VI. CONCLUSIONS

Four drive laps through the urban canyon showed visual and statistical similarity in the angular and delay spectra. In NLOS scenarios there is a tendency toward absolute delay biases on the order of tens of meters, but delay biases that are not sensitive to meter-level offsets in lateral and longitudinal position. Angular spectra are dominated by the surrounding building geometry, and the peaks of the received power spectra have little correlation with the actual receiver-transmitter geometry for such scenarios when direct transmission is heavily attenuated.

The moderate success of the Convolutional Neural Network in generating fingerprint-based estimations of both position and heading at 75 millisecond intervals also shows that there is promise in this channel representation. Fingerprints can represent
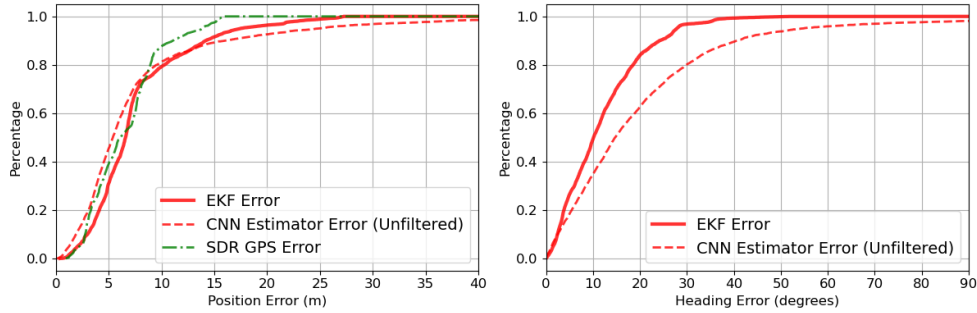
Figure 8: Cumulative distribution functions of CNN estimator errors. (Left) Filtered and unfiltered position errors. (Right) Filtered and unfiltered heading errors.

more than just position, angular information can be taken into consideration as well when antenna arrays are utilized. Even with a single transmitting antenna, multipath reflection is shown to be effective at providing a basis for orientation estimation, which is desirable for many problems in navigation. Performance shown by the test system, for a challenging scenario, was similar to that of an unaugmented GPS L1 receiver, but with the benefits of a faster update rate and independent heading updates in the UE frame.

Matched filter representation of the channel allows for the preservation of information that might otherwise be lost if representing the channel as the summation of a discrete number of plane waves, and can reduce the complexity of performing a computationally intensive super resolution algorithm.

In the future, it would be interesting to integrate multiple sectors and multiple eNodeBs into the estimation, to investigate the sensitivity of such a representation to absolute timing error, and to add memory to the neural network rather than filtering neural network outputs with a Kalman filter.

ACKNOWLEDGEMENTS

REFERENCES

Aditya, S., Molisch, A. F., and Behairy, H. M. (2018). A Survey on the Impact of Multipath on Wideband Time-of-Arrival-Based Localization. *Proceedings of the IEEE*, 106(7):1183–1203.

Burghal, D., Ravi, A. T., Rao, V., Alghafis, A. A., and Molisch, A. F. (2020). A Comprehensive Survey of Machine Learning Based Localization with Wireless Signals.

Dahlman, E., Parkvall, S., and Skold, J. (2013). *LTE/LTE-Advanced for Mobile Broadband*. Academic Press.

del Peral-Rosado, J. A., Raulefs, R., López-Salcedo, J. A., and Seco-Granados, G. (2017). Survey of cellular mobile radio localization methods: From 1G to 5G. *IEEE Communications Surveys & Tutorials*, 20(2):1124–1148.

Dwivedi, S., Shreevastav, R., Munier, F., Nygren, J., Siomina, I., Lyazidi, Y., Shrestha, D., Lindmark, G., Ernström, P., Stare, E., et al. (2021). Positioning in 5G networks. *IEEE Communications Magazine*, 59(11):38–44.

Gentner, C., Jost, T., Wang, W., Zhang, S., Dammann, A., and Fiebig, U.-C. (2016). Multipath Assisted Positioning with Simultaneous Localization and Mapping. *IEEE Transactions on Wireless Communications*, 15(9):6104–6117.

Kassas, Z., Khalife, J., Shamaei, K., and Morales, J. (2017). I Hear, Therefore I Know Where I Am: Compensating for GNSS Limitations with Cellular Signals. *IEEE Signal Processing Magazine*, 34(5):111–124.

Landmann, M. and Del Galdo, G. (2004). Efficient Antenna Description for MIMO Channel Modelling and Estimation. In *7th European Conference on Wireless Technology, 2004.*, pages 217–220. IEEE.

Luo, Y., Hsu, L.-T., and Pan, Y. (2021). A Super-Resolution Algorithm with FRFT Towards GNSS TOA Estimation for Multipath

Channel. In *Proceedings of the 34th International Technical Meeting of the Satellite Division of The Institute of Navigation (ION GNSS+ 2021)*, pages 3350–3359.

Müller, P., del Peral-Rosado, J. A., Piche, R., and Seco-Granados, G. (2016). Statistical Trilateration With Skew-t Distributed Errors in LTE Networks. *IEEE Transactions on Wireless Communications*, 15(10):7114–7127.

Niitsoo, A., Edelhäußer, T., Eberlein, E., Hadaschik, N., and Mutschler, C. (2019). A Deep Learning Approach to Position Estimation from Channel Impulse Responses. *Sensors*, 19(5):1064.

Orabi, M., Abdallah, A. A., Khalife, J., and Kassas, Z. M. (2021). A Machine Learning Multipath Mitigation Approach for Opportunistic Navigation with 5G Signals. In *Proceedings of the 34th International Technical Meeting of the Satellite Division of The Institute of Navigation (ION GNSS+ 2021)*, pages 2895–2909.

Sangodoyin, S., Kristem, V., Bas, C. U., Käske, M., Lee, J., Schneider, C., Sommerkorn, G., Zhang, C. J., Thomä, R., and Molisch, A. F. (2018). Cluster Characterization of 3D MIMO Propagation Channel in an Urban Macrocellular Environment. *IEEE Transactions on Wireless Communications*, 17(8):5076–5091.

Shamaei, K., Khalife, J., and Kassas, Z. M. (2018). A Joint TOA and DOA Approach for Positioning with LTE Signals. In *2018 IEEE/ION Position, Location and Navigation Symposium (PLANS)*, pages 81–91.

Strandjord, K., Morton, Y., and Wang, P. (2021). Evaluating the Urban Signal Environment for GNSS and LTE Signals. In *Proceedings of the 34th International Technical Meeting of the Satellite Division of The Institute of Navigation (ION GNSS+ 2021)*, pages 2166–2182.

Ulmschneider, M., Gentner, C., and Dammann, A. (2021). Cooperative Estimation of Maps of Physical and Virtual Radio Transmitters. In *Proceedings of the 34th International Technical Meeting of the Satellite Division of The Institute of Navigation (ION GNSS+ 2021)*, pages 2307–2317.

Vieira, J., Leitinger, E., Sarajlic, M., Li, X., and Tufvesson, F. (2017). Deep Convolutional Neural Networks for Massive MIMO Fingerprint-Based Positioning. In *2017 IEEE 28th Annual International Symposium on Personal, Indoor, and Mobile Radio Communications (PIMRC)*, pages 1–6. IEEE.

Wang, P. and Morton, Y. J. (2020). Multipath Estimating Delay Lock Loop for LTE Signal TOA Estimation in Indoor and Urban Environments. *IEEE Transactions on Wireless Communications*, 19(8):5518–5530.

Wang, P. and Morton, Y. J. (2020). Performance comparison of time-of-arrival estimation techniques for LTE signals in realistic multipath propagation channels. *NAVIGATION: Journal of the Institute of Navigation*, 67(4):691–712.